

Experimental measurement and Reynolds-averaged Navier-Stokes modelling of the near-field structure of multi-phase CO2 jet releases

R.M. Woolley, Michael Fairweather, C.J. Wareing, S.A.E.G. Falle, Christophe Proust, Jérôme Hebrard, Didier Jamois

▶ **To cite this version:**

R.M. Woolley, Michael Fairweather, C.J. Wareing, S.A.E.G. Falle, Christophe Proust, et al.. Experimental measurement and Reynolds-averaged Navier-Stokes modelling of the near-field structure of multi-phase CO2 jet releases. International Journal of Greenhouse Gas Control, 2013, 18, pp.139-149. 10.1016/j.ijggc.2013.06.014 . ineris-00961810

HAL Id: ineris-00961810
https://ineris.hal.science/ineris-00961810

Submitted on 20 Mar 2014

HAL is a multi-disciplinary open access archive for the deposit and dissemination of scientific research documents, whether they are published or not. The documents may come from teaching and research institutions in France or abroad, or from public or private research centers.

L'archive ouverte pluridisciplinaire **HAL**, est destinée au dépôt et à la diffusion de documents scientifiques de niveau recherche, publiés ou non, émanant des établissements d'enseignement et de recherche français ou étrangers, des laboratoires publics ou privés.

Experimental Measurement and Reynolds-Averaged Navier-Stokes Modelling of the Near-Field Structure of Multi-phase CO_2 Jet Releases

R.M. Woolley[a], M. Fairweather[b], and C.J. Wareing[c],

[abc]Institute of Particle Science and Engineering,
School of Process, Environmental and Materials Engineering,
University of Leeds, Leeds LS2 9JT, UK
[a]r.m.woolley@leeds.ac.uk (corresponding author)
Tel: +44 (0) 113 343 2351
Fax: +44 (0) 113 343 2384
[b]m.fairweather@leeds.ac.uk
[c]c.j.wareing@leeds.ac.uk

S.A.E.G. Falle[d]

[d]Department of Applied Mathematics,
School of Mathematics,
University of Leeds, Leeds LS2 9JT, UK
[d]s.a.e.g.falle@leeds.ac.uk

C. Proust[e], J. Hebrard[f], and D. Jamois[g]

[efg]INERIS, Dept. PHDS,
Parc Technologique ALATA,
BP 2, 60550 Verneuil-en-Halatte, France
[e]christophe.proust@ineris.fr
[f]jerome.hebrard@ineris.fr
[g]didier.jamois@ineris.fr

Submission of a full-length article to International Journal of Greenhouse Gas Control of unpublished material not submitted for publication elsewhere

Running title: Measurement and Prediction of Multi-phase CO_2 Releases

ABSTRACT

The deployment of a complete carbon capture and storage chain requires a focus upon the hazards posed by the operation of CO_2 pipelines and intermediate storage vessels, and the consequences of accidental release. The aim of this work is the construction of a computational fluid dynamic model capable of accurately representing the complex physics observed in such a release, essential if dispersion phenomena are to be accurately predicted. The interacting thermo-physical processes observed include those associated with the rapid expansion of a highly under-expanded jet, leading to an associated sonic flow structure. In such a release, it is also possible for three phases to be present due to the expansion and subsequent Joule-Thomson cooling, and a suitable equation of state is required to elucidate a system's composition. The primary objective of this work is the consideration of these physical processes, and their integration into a suitable numerical framework which can be used as a tool for quantifying associated hazards. This also incorporates the validation of such a model using data available in the literature and also using that recently obtained, and presented here for the first time. Overall, the model has provided an excellent level of agreement with experimental data in terms of fluid and sonic structure and temperature measurements, and good agreement with respect to composition data.

KEYWORDS

CCS, multi-phase flow, experimental measurement, mathematical modelling, accidental releases, atmospheric dispersion

1. INTRODUCTION

Carbon capture and storage (CCS) refers to a set of technologies designed to reduce carbon dioxide emissions from large point-sources of production such as coal-fired power stations and other industrial facilities, in order to mitigate greenhouse gas release. CCS technology involves capturing CO_2 and then storing it in a suitable semi-permanent facility such as naturally formed saline aquifers or depleted oil wells, instead of allowing its release to the atmosphere where it contributes to climate change.

The technological requirements for the safe transportation of large quantities of liquids and gases at high pressures have been established over a number of years. Put into practice, the technology is proven for a number of hazardous substances including combustibles and toxins. Now however, with the advent of large-scale carbon capture and storage projects, attentions have turned to the safe transportation and handling of dense-phase carbon dioxide (CO2PipeHaz, 2009). The physics observed during the high-pressure release of combustibles such as natural gas are well studied and their behaviours relatively well understood. However, CO_2 poses a number of dangers upon release due to its more unusual physical properties, the physics of which have not yet been fully elucidated. Currently, the work being undertaken in the CO2PipeHaz project (CO2PipeHaz, 2009) is pivotal to quantifying all the hazard consequences associated with CO_2 pipeline failure, forming the basis for emergency response planning and determining minimum safe distances to populated areas. Such pipelines are considered to be the most likely method for transportation of captured CO_2 from power plants and other industries prior to subsequent storage, and their safe operation is of paramount importance as their inventory is likely to be several thousand tonnes.

CO_2 is a colourless and odourless asphyxiant which is directly toxic if inhaled in air at concentrations around 5%, and is likely to be fatal at concentrations around 10% (NIOSH, 1996). Liquid CO_2 has a density much greater than water, but has a viscosity of magnitude more frequently associated with gases, and these properties make the transport of CO_2 an economically viable and attractive proposition. However, preliminary calculations and experimental evidence indicate that, due to it possessing a relatively high Joule-Thomson expansion coefficient, the rapid expansion of an accidental release may reach temperatures below -180 K. Due to this effect, solid formation following a pipeline puncture or rupture is to be expected, whether directly from liquid or via a vapour-solid phase transition with the passing of the system through the triple point (216.6 K at 5.11 atm). Additionally, CO_2

sublimes at ambient atmospheric conditions, which is behaviour not seen in most other solids. This is an important consideration when assessing the hazards posed by accidental releases, as CO_2 is denser than air, and an evaporating pool formed by liquid rain-out or a subliming solid deposit could cause a density-driven flow of high CO_2 concentration at ground level, in addition to the hazard posed by the associated gaseous release.

The developments presented in this paper describe a novel multi-phase discharge and dispersion model capable of predicting both the near- and far-field turbulent fluid dynamics and phase-transition phenomena associated with accidental CO_2 releases. As previously discussed, predicting the correct thermodynamic phase during the discharge process in the near-field is of particular importance given the very different hazard profiles of CO_2 in the gas and solid states. The modelling of CO_2 fluid dynamics therefore poses a unique set of problems, and the theoretical developments presented in this paper go some way to elucidating the observed physics. Previous works concerned with the near-field modelling of CO_2 releases are well covered in a recent review (Dixon et al., 2012), and should be consulted for other recent developments.

Also presented are the results of a series of experimental measurements of large-scale jet-releases of CO_2, representative of pipeline punctures under various conditions. This series of experiments represents the most up-to-date data set available, describing the temperature and concentration fields of such under-expanded flows. Model validations have also been undertaken using the experimental data described, with shortcomings of the mathematical model elucidated through such comparisons, and suggestions for further developments presented.

It should also be noted that the modelling work presented here has further possible applications, and not solely within the field of CO_2 pipeline safety. Although the techniques used for the modelling of sonic jets are widely reported upon, the representation of the three-phase CO_2 expansion and the associated thermo-physical phenomena is a novel approach. This could be applied in a number of areas of technology including those based upon the Rapid Expansion of Supercritical Solvents (RESS) processes including pharmaceutical, cosmetic, and speciality chemical industries. In these applications, the geometry of particles produced is determined by a number of factors including nozzle geometry, mass flow-rate, and pressure and temperature of CO_2. Hence, an ability to model and predict fluid structures and particle distributions would be a great benefit in the design stage of such processes.

2. EXPERIMENTAL ARRANGEMENT

Figure 1 depicts a schematic of the rig used at INERIS for the experimental studies of large-scale CO_2 releases. In the modelled region of the flow field, the instrumentation consists of fifteen radially distributed thermocouples, and three oxygen sensors distributed along the centre-line axis of the jet. The region used for the model validation extends to 5m from the release plane and is indicated by the shaded area of Figure 1. The choice of the modelling domain size is due to the model developments in this paper being concerned with the accurate representation of under-expanded, shock-laden, multi-phase jets, and the structure of their near-field. By 5m downstream of the release point, the jet has become self-similar in its properties, and has been at atmospheric pressure for a considerable distance. Hence, the modelling of this region does not require such specialist treatment.

Figure 2 is a photograph of the same rig, showing the external release point on the right of the picture, and the refilling sphere in-situ in front of the main vessel. The latter 2 cubic metre spherical pressure vessel is thermally insulated, and can contain up to 1000 kg of CO_2 at a maximum operating pressure and temperature of 200 bar and 473 K, respectively. It is equipped internally with 6 thermocouples and 2 high-precision pressure gauges as well as sapphire observation windows. It is connected to a discharge line of 50 mm inner diameter, with no internal restrictions. In total, the line is 9 metres long including a bend inside the vessel, plunging to the bottom in order to ensure that it is fully submersed in liquid CO_2. Three full-bore ball valves are installed in the pipe. Two are positioned close to the vessel and the third near to the orifice holder. The first valve closest to the sphere is a manual safety valve, and the two others are remotely actuated.

The vessel is supported by 4 load cells enabling a continuous measurement of the CO_2 content. The determination of the mass flow rate is performed within an accuracy of approximately 10%. The temperature is measured inside the vessel and immediately upstream of the orifice with 0.5 mm K-type thermocouples of accuracy better than 1 K. The static pressure is measured inside the vessel using a Kistler 0-200 bar instrument with an accuracy of ±0.1%, and immediately upstream from the orifice using a KULITE 0-350 bar instrument with an accuracy of ±0.5%. The vessel instrumentation is shown in Figure 3.

Various orifices can be and were used at the exit plane of the discharge pipe, and are all drilled into a large screwed flange. The thickness of this flange is typically 15 mm and the

diameter of the orifice is constant over a length of 10 mm and then expanded with an angle of 45° towards the exterior. Figure 4 provides an example of such an orifice, whilst Figure 5 is a high-speed camera still of a typical release from a 9 mm nozzle. The discharge nozzle diameters used were 6, 9, 12 and 25mm in the six tests reported and studied here.

The field instrumentation consists of K-type thermocouples (0.5 mm diameter) arranged on vertical masts at varying distances from the orifice. The response time of these is approximately 1 second. Additionally, at each mast there is an O_2 sensor located on the centre-line of the jet.

A number of experimental configurations have been investigated during the project, but the most recent data are presented here. The details of six release scenarios, typical of CO_2 transport conditions, are presented in Table 1, which are used for the model validation.

3. MATHEMATICAL MODELLING

3.1 Governing Equations

Predictions were based on the solutions of the Reynolds-averaged, density-weighted forms of the transport equations for mass, momentum, two conserved scalars (CO_2 mass fraction and CO_2 dense phase fraction), and total energy per unit volume (internal energy plus kinetic energy), as described below by Equations 1, 2, 3, 4, and 5 respectively. This model is capable of representing a fluid flow-field comprising a mixture of CO_2 (vapour/liquid/solid) and air. The equations employed in this study were cast in an axisymmetric geometry, but for brevity all subsequent equations are listed in their Cartesian tensor form.

$$\frac{\partial \overline{\rho}}{\partial t} + \frac{\partial}{\partial x_i}\left(\overline{\rho}\tilde{u}_i\right) = 0 \tag{1}$$

$$\frac{\partial}{\partial t}\left(\overline{\rho}\tilde{u}_i\right) + \frac{\partial}{\partial x_j}\left(\overline{\rho}\tilde{u}_i\tilde{u}_j + \overline{p} - \overline{\rho}\widetilde{u_i''u_j''}\right) - s_u = 0 \tag{2}$$

$$\frac{\partial}{\partial t}\left(\overline{\rho}\tilde{\beta}\right) + \frac{\partial}{\partial x_i}\left(\overline{\rho}\tilde{\beta}\tilde{u}_i\right) - \frac{\partial}{\partial x_i}\left[\mu_t \frac{\partial \tilde{\beta}}{\partial x_j}\right] = 0 \tag{3}$$

$$\frac{\partial}{\partial t}\left(\overline{\rho}\tilde{\alpha}\right) + \frac{\partial}{\partial x_i}\left(\overline{\rho}\tilde{\alpha}\tilde{u}_i\right) - \frac{\partial}{\partial x_i}\left[\mu_t \frac{\partial \tilde{\alpha}}{\partial x_j}\right] - s_\alpha = 0 \tag{4}$$

$$\frac{\partial \tilde{E}}{\partial t} + \frac{\partial}{\partial x_i}\left[(\tilde{E} + \overline{p})\tilde{u}_i - \tilde{u}_i\widetilde{u_i''u_j''}\right] - \frac{\partial}{\partial x_i}\left(\mu_t T \frac{\partial S}{\partial x_j}\right) - s_E = 0 \tag{5}$$

This equation set is closed via the prescription of the turbulence stress tensor ($\widetilde{u_i''u_j''}$) as prescribed in Section 3.2.

3.2 Turbulence Modelling

Closure of the equation set discussed in Section 3.1 was achieved via the $k-\varepsilon$ turbulence model (Jones and Launder, 1972), where $\widetilde{u_i''u_j''}$ are the Reynolds stresses, and are modelled using this approach as:

$$\overline{\rho}\widetilde{u_i''u_j''} = \frac{2}{3}\delta_{ij}\left(\overline{\rho}k + \mu_t\frac{\partial\tilde{u}_k}{\partial x_k}\right) - \mu_t\left(\frac{\partial\tilde{u}_l}{\partial x_j} + \frac{\partial\tilde{u}_j}{\partial x_l}\right) \tag{6}$$

Here, the turbulent or eddy viscosity is represented as a function of the turbulence kinetic energy by:

$$\mu_t = C_\mu\overline{\rho}\frac{k^2}{\varepsilon} \quad \text{with} \quad C_\mu = 0.09 \tag{7}$$

which leaves the requirement for the solution of transport equations for the turbulence kinetic energy and its dissipation rate. Subsequently, these are modelled as:

$$\frac{\partial}{\partial t}\left(\overline{\rho}k\right) + \frac{\partial}{\partial x_i}\left(\overline{\rho}k\tilde{u}_i\right) - \frac{\partial}{\partial x_i}\left[\mu_t\frac{\partial k}{\partial x_i}\right] - s_k = 0 \tag{8}$$

and

$$\frac{\partial}{\partial t}\left(\overline{\rho}\varepsilon\right) + \frac{\partial}{\partial x_i}\left(\overline{\rho}\varepsilon\tilde{u}_i\right) - \frac{\partial}{\partial x_i}\left[\mu_\varepsilon\frac{\partial\varepsilon}{\partial x_i}\right] - s_\varepsilon = 0 \quad \text{with} \quad \mu_\varepsilon = \frac{\mu_t}{1.3} \tag{9}$$

where the source terms s_k and s_ε are defined as:

$$s_k = P_t - \overline{\rho}\varepsilon \quad \text{and} \quad s_\varepsilon = \frac{\varepsilon}{k}\left(C_1P_t - C_2\overline{\rho}\varepsilon\right) \tag{10}$$

$$\text{with } C_1 = 1.4 \quad \text{and} \quad C_2 = 1.94 \tag{11}$$

and

$$P_t = \mu_t\left[\frac{\partial\tilde{u}_i}{\partial x_j}\left(\frac{\partial\tilde{u}_i}{\partial x_j} + \frac{\partial\tilde{u}_j}{\partial x_i}\right)\right] - \frac{2}{3}\frac{\partial\tilde{u}_i}{\partial x_i}\left(\overline{\rho}k + \mu_t\frac{\partial\tilde{u}_j}{\partial x_j}\right) \tag{12}$$

Although the standard *k-ε* model has been extensively used for the prediction of incompressible flows, its performance is well known to be poor in the prediction of their compressible counterparts. The model consistently over-predicts turbulence levels and hence mixing due to compressible flows displaying an enhancement of turbulence dissipation. A number of modifications to the *k-ε* model have been proposed by various authors, which include corrections to the constants in the turbulence energy dissipation rate equation (Baz, 1992; Chen and Kim, 1987), and to the dissipation rate itself (Sarkar et al., 1991; Zeman,

1990). Previous works by the present author (Fairweather and Ranson, 2003, 2006) have indicated that for flows typical of those being studied here, the model proposed by Sarkar et al. (Sarkar et al., 1991) provides the most reliable predictions. This model specifies the total dissipation as a function of a turbulent Mach number and was derived from the analysis of a direct numerical simulation of the exact equations for the transport of the Reynolds stresses in compressible flows. Observations made of shock-containing flows indicated that the important sink terms in the turbulence kinetic energy budget generated by the shocks were a compressible turbulence dissipation rate, and to a lesser degree, the pressure-dilatation term. In isotropic turbulent flow, the pressure-dilatation term was found to be negligibly small, and so it was proposed that the compressible dissipation rate take the form:

$$\varepsilon_c = CM_t^2 \varepsilon \tag{13}$$

where the constant C is set to unity to allow for the neglected pressure-dilatation term and M_t is the turbulent Mach number. The application to the *k-ε* model is then made by modification to the source term of the turbulence energy evolution equation and to the turbulence viscosity as defined by Equations (14) and (15) respectively:

$$s_k = -\overline{\rho} M_t^2 \varepsilon \tag{14}$$

$$\mu_t = C_\mu \rho \frac{k^2}{(1+M_t^2)\varepsilon} \tag{15}$$

The turbulent Mach number is defined as:

$$M_t = \frac{(2k)^{1/2}}{c} \tag{16}$$

where c is the local speed of sound.

Figure 6 demonstrates the effect of these modifications upon the axial centre-line velocity profile predictions of a highly under-expanded air jet, reported by (Donaldson and Snedeker, 1971). The standard *k-ε* model is clearly too dissipative, leading to an early decay of the compression/decompression cycle. The compressibility corrected model, although remaining unable of describing the magnitude of the velocity at the peak of the second decompression cycle, evidently improves agreement with experimental observation by reducing the spreading rate of the jet.

3.3 Fluid Properties and Species Transport

3.3.1 Non-ideal Equation of State

The Peng-Robinson equation of state (Peng and Robinson, 1976) is satisfactory for predicting the gas phase properties of CO_2, but when compared to that of Span and Wagner (Span and Wagner, 1996), it is not so for the condensed phase. Furthermore, it is not accurate for gas pressures below the triple point and, in common with any single equation, it does not account for the discontinuity in properties at the triple point. In particular, there is no latent heat of fusion.

Span and Wagner (Span and Wagner, 1996) give a formula for the Helmholtz free energy that is valid for both the gas and liquid phases above the triple point, but it does not take account of experimental data below the triple point, nor does it give the properties of the solid. In addition, the formula is too complicated to be used efficiently in a computational fluid dynamics code. A composite equation of state has therefore been constructed to determine the phase equilibrium and transport properties for CO_2. The inviscid version of this model is presented in detail elsewhere (Wareing et al., 2013) and the method reviewed here is now extended for the turbulent closure of the fluid equations detailed in the previous section. In this, the gas phase is computed from the Peng-Robinson equation of state (Peng and Robinson, 1976), and the liquid phase and saturation pressure are calculated from tabulated data generated with the Span and Wagner (Span and Wagner, 1996) equation of state and the best available source of thermodynamic data for CO_2, the Design Institute for Physical Properties (DIPPRR) 801 database, access to which can be gained through the Knovel library (DIPPR, 2013).

The properties of gaseous CO_2 are obtained from the Peng-Robinson equation of state, where the pressure is defined as:

$$P = \frac{RT}{(v-b)} - \frac{\delta a(T)}{v(v+b)+b(v-b)} \tag{17}$$

where T is the temperature, R the Universal gas constant, and v is the molar volume. The parameters a and b are given to be:

$$a = 0.45724\frac{(RT_{crit})^2}{p_{crit}} \quad \text{and} \quad b = 0.07780\frac{RT_{crit}}{p_{crit}} \tag{18}$$

with

$$\delta = \left[1 + \left(0.37464 + 1.54226\omega - 0.26992\omega^2\right)\left(1 - \sqrt{\frac{T}{T_{crit}}}\right)\right]^2 \tag{19}$$

In Equations (18) and (19), the critical temperature, pressure, and acentric factor associated with CO_2 are given as:

$$p_{crit} = 7.3773 \times 10^6\ Pa, \quad T_{crit} = 304.1282\ K \quad \text{and} \quad \omega = 0.228 \tag{20}$$

The internal energy in the gas phase is computed using the following expression for the specific heat at constant volume:

$$C_v = A + BT + CT^2 \tag{21}$$

where $A = 469.216$, $B = 0.6848$, and $C = 1.211 \times 10^{-4}$. This expression has been obtained by fitting to the internal energy data in the DIPPR database (DIPPR, 2013) over the temperature range $150 \le T\left(K\right) \le 300$. The internal energy of the gas at the reference state used by Span and Wagner (STP) is then:

$$U = 1.71403 \times 10^5\ J\ kg^{-1} \tag{22}$$

The internal energy of the liquid is taken from Span and Wagner (Span and Wagner, 1996), except that $1.4422 \times 10^4\ J\ kg^{-1}$ is added to the values in order to ensure that differences between the gas and liquid internal energies on the saturation line in the model are in agreement. The solid internal energy is described as:

$$U = -4.04533 \times 10^5 + A\left(T - T_t\right) + B\frac{\left(T^2 - T_t^2\right)}{2} + C\frac{\left(T^3 - T_t^3\right)}{3}\ J\ kg^{-1} \tag{23}$$

where $A = -36.4215$, $B = 12.3027$, and $C = 0.02882$. This has been obtained from the DIPPRR Database tables along with the latent heat of fusion at the triple point of $2.04932 \times 10^5\ J\ kg^{-1}$. Note that the pressure dependence and the difference between the internal energy and the enthalpy for the solid are ignored since these are negligible.

To calculate the solid density, the same approach as Witlox et al. (Witlox et al., 2009) is used, and expressed as:

$$\rho = 1289.45 + 1.8325T \; kg\, m^{-3} \tag{24}$$

again based on property information from the DIPPRR 801 Database. From Liu (Liu, 1984), the solid sound speed at atmospheric pressure and $296.35\,K$ is $1600\,m\,s^{-1}$ and it is assumed that this is independent of temperature and pressure. Note that the results given below are extremely insensitive to the solid density and sound speed.

The saturation pressure above the triple point is taken from Span and Wagner (1996). Below the triple point, they give the following empirical formula:

$$p_s(T) = p_t \exp\left\{\left[a_1\left(1.0-\frac{T}{T_t}\right)+a_2\left(1.0-\frac{T}{T_t}\right)^{1.9}+a_3\left(1.0-\frac{T}{T_t}\right)^{2.9}\right]\frac{T_t}{T}\right\} Pa \tag{25}$$

where $T_t = 216.592\,K$ is the temperature of the triple point, $p_t = 0.51795\times10^6\,Pa$ is the pressure at the triple point and $a_1 = -14.740846$, $a_2 = 2.4327015$, and $a_3 = -5.3061778$. Figure 7 shows the internal energy of the gas and condensed phases on the saturation line. The transition from liquid to solid has been smoothed over $4\,K$ with a hyperbolic tangent function centred on the triple point. This has been done for computational reasons in order to ensure the function and its differentials are smooth.

When working with an equation of state, it is convenient to use the Helmholtz free energy (*H*) in terms of temperature and molar volume as all other thermodynamic properties can be readily obtained from it. For an ideal gas, the Hemholtz free energy per mole is given by:

$$H = H_i = -RT\left[\frac{1}{(\gamma-1)}\ln\left(\frac{T}{T_0}\right)+\ln\left(\frac{v}{v_0}\right)\right] \tag{26}$$

where T_0 and v_0 are reference states at which the ideal equation of state is valid. In the present non-ideal case, we can use the standard relation describing pressure:

$$p = -\left(\frac{\partial H}{\partial v}\right)_T \tag{27}$$

to obtain the Hemholtz free energy from any equation of state as:

$$H(T,v) = H_i(T,v_0) - \int_{v_0}^{v} p\,d\,\text{ا} \tag{28}$$

With a definition for the Helmholtz free energy, the entropy is obtained from the relation:

$$S = -\left(\frac{\partial H}{\partial T}\right)_v \tag{29}$$

and the internal energy is then given by:

$$U(T,v) = H + TS = H - T\left(\frac{\partial H}{\partial T}\right) \tag{30}$$

The local speed of sound, required by Equation (16) to construct the turbulent Mach number can now be derived. Using standard relations, it can be shown that:

$$\left(\frac{\partial p}{\partial v}\right)_S = \left(\frac{\partial p}{\partial v}\right)_T - \left(\frac{\partial p}{\partial T}\right)_v \left(\frac{\partial S}{\partial v}\right)_T \left(\frac{\partial S}{\partial T}\right)_v^{-1} \tag{31}$$

and:

$$c = \left[\left(\frac{\partial p}{\partial \rho}\right)_S\right]^{1/2} \left[-v^2\left(\frac{\partial p}{\partial v}\right)_S\right]^{1/2} \tag{32}$$

3.3.2 Homogeneous Equilibrium Model

In a homogeneous equilibrium model (HEM), all phases are assumed to be in dynamic and thermodynamic equilibrium. *Id est* they all move at the same velocity and have the same temperature. In addition, the pressure of the CO_2 vapour is assumed to be equal to the saturation pressure whenever the condensed phase is present. The pressure of the condensed phase CO_2 is assumed to be equal to the combined pressure of CO_2 vapour and air (the total pressure). These assumptions are reasonable provided the CO_2 liquid drops or solid particles are sufficiently small so that they do not interact with the gas-phase turbulence

As the code employed in this work is conservative, it works with the total energy per unit volume as given by Equation 5, and also computes the total mass fraction of CO_2 (β) via Equation 3. In order to integrate the conservation equations, it is also necessary to calculate the total pressure, temperature, total mass fraction of CO_2, density of CO_2 vapour, density of air, and density of condensed phase CO_2, from the total density, U, and β.

In unit volume, the mass of the condensed phase CO_2 is then:

$$m_l = \alpha\beta\rho \tag{33}$$

which means the volume of the condensed phase CO_2 is:

$$V_l = \frac{\alpha\beta\rho}{\rho_l} \tag{34}$$

The volume of the combined vapour and air is then:

$$V_g = 1 - V_l = 1 - \frac{\alpha\beta\rho}{\rho_l} \tag{35}$$

Since the masses of the vapour and air per unit volume are:

$$m_v = \beta(1-\alpha)\rho \quad \text{and} \quad m_a = (1-\beta)\rho \tag{36}$$

their densities are then:

$$\rho_v = \frac{m_v}{V_g} = \frac{\beta(1-\alpha)\rho}{\left(1 - \frac{\alpha\beta\rho}{\rho_l}\right)} \tag{37}$$

and

$$\rho_a = \frac{m_a}{V_g} = \frac{(1-\beta)\rho}{\left(1 - \frac{\alpha\beta\rho}{\rho_l}\right)} \tag{38}$$

Since the CO_2 vapour is in equilibrium with the solid/liquid CO_2, the following holds:

$$p_s(T) = p\left(\frac{m_v}{\rho_v}, T\right) \tag{39}$$

where $p(\rho_v, T)$ is the pressure given by the equation of state, Equation (17). In regions where there is significant mixing, one can use the ideal equation of state for the CO_2 vapour and:

$$p\left(\rho_v, T\right) = \frac{R\rho_v T}{m_v} \tag{40}$$

The total pressure is then given by:

$$p = RT\left(\frac{\rho_a}{m_a} + \frac{\rho_v}{m_v}\right) \tag{41}$$

and the total internal energy by:

$$U = RT\left[\frac{\beta\left(1-\alpha\right)}{m_v\left(\gamma_v - 1\right)} + \frac{\left(1-\beta\right)}{m_a\left(\gamma_a - 1\right)}\right] + \alpha\beta U\left(\rho_l, T\right) \tag{42}$$

where $U\left(\rho_l, T\right)$ is the internal energy per unit mass of condensed phase CO_2. The solid density is then determined from:

$$\rho_l = \rho_l\left(p, T\right) \tag{43}$$

which is obtained from the equation of state. Equations (33) to (38) are solved for T, p, and α using a Newton-Raphson iteration.

3.3.3 Homogeneous Relaxation Model

As previously discussed, the assumptions associated with the HEM are reasonable provided the CO_2 liquid drops or solid particles are sufficiently small. There are some indications that this will not be true, in particular for test calculations in which the release is from a nozzle with a diameter of the order of centimetres. Hence, the model was further developed as a homogeneous relaxation model, in that a relaxation time was introduced with respect to the transport of the dense phase. It was found that this extension to the model had significant effect upon predictions, and was required to effect the more accurate results presented in Section 4.

A full model requires the inclusion of discrete drops or particles, but it is possible to derive a simple sub-model for the relaxation to equilibrium in which the temperature relaxation is ignored and it is simply assumed that the condensed phase mass fraction is given by Equation 4 with the following source term:

$$s_\alpha = \beta \frac{(p_v - p_s)}{\tau p_s} \tag{44}$$

and where p_v is the vapour pressure, p_s the saturation pressure, and τ the relaxation time. This is consistent with the form of the evaporation/condensation rate given in Jacobson (Jacobson, 1999). The relaxation time chosen to represent behaviour in the near-field of releases such as those considered herein was in the order of 10^{-3} s and obtained by the assessment of the rate that the calculated CO_2 saturation pressure relaxed to the local vapour pressure. In post-shock regions of the flow, a relaxation time of the order 2.5 s was chosen, representing the non-equilibrium state of the condensed phase.

3.4 Discretisation and Mesh Adaption

Solutions of the time-dependent, axisymmetric forms of the descriptive equations were obtained using a modified version of a general-purpose fluid dynamics code referred to as MG, and provided by Mantis Numerics Ltd. Within this code, integration of the equations employed a second-order accurate, upwind, finite-volume scheme in which the transport equations were discretised following a conservative control-volume approach, with values of the dependent variables being stored at the computational cell centres. Approximation of the diffusion and source terms was undertaken using central differencing, and a Harten, Lax, van Leer (HLL) (Harten et al., 1983) second-order accurate variant of Godunov's method applied with respect to the convective and pressure fluxes. The fully-explicit, time-accurate method was a predictor-corrector procedure, where the predictor stage is spatially first-order, and used to provide an intermediate solution at the half-time between time-steps. This is then subsequently used at the corrector stage for the calculation of the second-order fluxes. A further explanation of this algorithm can be found elsewhere (Falle, 1991).

The calculations also employed an adaptive finite-volume grid algorithm (Falle and Giddings, 1993) which uses a two-dimensional rectangular mesh with grid adaption achieved by the successive overlaying of refined layers of computational mesh. Figure 8 demonstrates this technique. Where there are steep gradients of variable magnitudes such as at flow boundaries or discontinuities such as the Mach disc, the mesh is more refined than in areas such as the free stream of the surrounding fluid. Each layer is generated from its predecessor by doubling the number of computational cells in each spatial direction. This technique enables the

generation of fine grids in regions of high spatial and temporal variation and, conversely, relatively coarse grids where the flow-field is numerically smooth. Hence, the code uses a hierarchy of grids, $G_0 \cdots G_N$ such that if the mesh spacing is Δx_n on grid G_n then it is $\Delta x_n/2$ on G_{n+1}. Grids G_0 and G_1 cover the entire domain, but finer grids only exist where they are required for accuracy. Unlike codes such as FLASH (Chicago, 2010) that use patches of fine grid, refinement is on a cell-by-cell basis. The solution is computed on all grids and refinement of a cell on G_n to G_{n+1} occurs whenever the difference between the solutions on G_{n-1} and G_n exceeds a given error. Again, unlike FLASH (Chicago, 2010), each grid is integrated at its own time-step.

With respect to the establishment of grid-independent solutions, all calculations reported upon here were undertaken using refined grids in which the magnitude of fractional difference between the solution on the uppermost grid and a next level of possible refinement was below 0.5%. It has been ascertained through the study of numerous calculations, that this level of refinement provides solutions which purport negligible differences to those obtained on higher-resolution grids. In the case of the under-expanded air-jet calculations reported upon in Section 3.2, this resulted in fully-refined axi-symmetric meshes containing in the region of 130,000 nodes at 5 levels of refinement. Comparing this to previous similar studies, a non-uniform axisymmetric grid was reported to provide grid-independent solutions at a resolution of 126,000 nodes (Birkby and Page, 2001); an adaptive technique, again used on an axisymmetric grid, reported similar success using 30,000 nodes (Bartosiewicz et al., 2002); and a full 3-dimensional model of a supersonic jet in a cross-flow was reported to be grid-independent using 1,544,098 cells (Viti and Schetz, 2005). Hence, the required level of refinement used in the present work appears to agree with that noted by previous authors. Additionally, it was found that the computational grids applied to the modelling of the CO_2 jets, required upwards of 500,000 nodes to achieve an independent solution. This was mainly due to the larger computational region which was required, extending to 5 metres downstream.

4. RESULTS AND DISCUSSION

The calculations required initial conditions of temperature, pressure, density, velocity, and dense-phase CO_2 mass fraction, which were obtained from isentropic decompression calculations of CO_2. Initial conditions for the decompression were prescribed from experimental observation of conditions within the storage sphere, and at the head of the release pipe, which was assumed smooth. A sensitivity analysis was undertaken as to the effect of nominal pipe-wall roughness, and negligible effect was observed upon the results. It was however observed that the accuracy of the predictions was notably affected by the initially prescribed flow rate.

Figure 9 shows predictions of temperature profiles plotted against experimental data for tests 2, 3, and 4, at axial locations of 1, 2, 3, 4, and 5 m, observed on the centre-line of the jets. The absence of data at the 1m position in test 2 is due to the freezing of the thermocouple and the consequent production of an erroneous signal. Additionally, Figure 9 compares predictions of O_2 molar concentration with experimental observation where data are available, namely centre-line locations in jets 2 and 3. These three tests were undertaken using the 6 mm nozzle, and data was only collected along the centre-line of the releases. The experimental sensor matrix was expanded in further tests to incorporate radial profiles, which will be subsequently discussed.

Predictions of axial temperatures of all three tests are in good agreement with observation, although an over-prediction of temperature in the near-field is observed in each. For tests 2 and 3, however, this over-prediction mostly lies within the limits of experimental error, but test 3 results show a slightly larger discrepancy at the one and two metre locations. This does however have the effect of bringing the far-field predictions at 2, 4, and 5 metres more into line with data. A slight change in gradient can be seen in the curve of predicted temperatures just before the axial location of 1 metre in all cases. This phenomena is to be expected, and is due to the system passing through the triple point as the temperature increases. The change in equilibrium from solid-gas to liquid-gas causes a change in the internal energy of the dense phase and hence effects a change in the local temperature. Additionally, predictions of O_2 concentrations along the centre-line of tests 2 and 3 are in good agreement with experiment. An over-prediction of mixing within the first two metres of the release is translated into a slight over-prediction of O_2 fractions, but the models' performance remains meritorious. O_2 data for test 4 were not available. The over-dissipative solution is indicative of an incorrectly

predicted mixing rate, and the k-ε turbulence model is well known to underperform in such a manner in compressible jets such as these. Although corrected according to the model of Sarkar et al. (1991) there is the possibility of an anisotropic element of the Reynolds-stress tensor not being accounted for, and hence a second-moment turbulence closure is currently being incorporated within the model framework to address this issue.

Figure 10 shows predictions of radial temperature profiles plotted against experimental data measured along a vertical line through the release for tests 6, 7, and 8, at axial locations of 1, 2 and 5 m. The model qualitatively and quantitatively captures the thermodynamic structure of the sonic releases, and although there is a small discrepancy between the observed and predicted spreading rates in the very near-field, calculations lie within the accepted error range of the experimental data. Within the core of the jets, temperatures are seen to be slightly under-predicted when compared to experiment, except in the predicted inviscid region still present at 1 metre in tests 6 and 7, and 2 metres in test 8. It is possible that dense phase CO_2 is removed from the system due to such phenomena as agglomeration, which would affect the higher temperatures observed. Hence, recent developments of the model include the incorporation of sub-models for the distribution of solid and liquid particles within the flow, and it is expected that the effects of phenomena such as particle coagulation will have an impact upon the predicted temperatures. Also, the system may not be in equilibrium due to this, or the generated turbulence, which may cause the observed discrepancies. The peaks locate the centre of the jets, where pure CO_2 is present in both solid, and vapour phases. The solid and vapour are in equilibrium here, and hence the CO_2 vapour pressure is equal to the CO_2 saturation pressure. The local temperature is thus defined by this condition in the model. The total pressure in this region is near to atmospheric and hence a high concentration of CO_2 will affect a higher local temperature. Moving away from the centre-line, and into a region of mixing, the CO_2 fraction is reducing, leading to a reduction in vapour pressure and hence a lowering of the temperature. Once no solids remain, there is an inflection in the curve and the temperature is seen to increase with the mixing of the CO_2 vapour and ambient air. By 2m in tests 6 and 7 and by 5 metres in test 8, there is no dense phase predicted as remaining and the temperature profile is determined by the mixing of CO_2 with air at atmospheric pressure. It should be noted that this centre-line peak in predicted temperatures appears to be a feature of the homogenous model applied in these calculations, and this numerical phenomena is not reproduced in experimental observation, although further more detailed measurements would be useful in this regard. It is anticipated that the

removal of the effect of the HEM assumption, and hence the formation of the troughs in the off-centre thermal profile, will go some way to bring predictions more in line with data. It is therefore expected that this will not be observed in calculations incorporating recently developed Lagrangian particle tracking models, which is the subject of further work being currently undertaken.

Figure 11 depicts axial profiles of temperature predictions plotted against experimental data along the centre-line in the CO_2 releases of tests 6, 7, and 8. As previously discussed, the level of agreement between calculation and experiment is comparable for these three investigations. Also reflected is the observed centre-line under-prediction of temperature common to tests 6 and 7. Figure 11 also displays predictions of O_2 molar fraction plotted against experimental data on the centre-line of the same tests. Contrary to calculations of tests 2, 3, and 4, an under-prediction of temperature in the near-field now leads to an associated under-prediction of O_2 fraction at the same locations. This under-prediction at the distance of 1metre in these investigations is however notably accentuated when compared to the previous experiments, and requires further investigation. According to (Birch et al., 1984), the axial concentration decay of an under-expanded jet release can be prescribed as:

$$\overline{\eta} = \frac{k d_{ps}}{z+n}\left(\frac{\rho_a}{\rho_g}\right)^{1/2} \tag{44}$$

where the pseudo-diameter is given by:

$$d_{ps} = d\sqrt{0.587 C_d \left(\frac{p_0}{p_a}\right)} \tag{45}$$

where 0.587 is a CO_2 dependent constant. The axial decay constant k is given a universal value of 4.90, and C_d a value of 0.85. This approach to the approximation of the mixing in tests 6, 7, and 8 was applied, and associated O_2 concentrations calculated. The crossed-circle symbols of Figure 11 show these values plotted against experimental observation and predicted results. Interestingly, the conformity of experimental observation and the prescription of (Birch et al., 1984), decreases with increasing nozzle size and initial reservoir pressure. It is also notable that the experimental data are in close agreement with the theory of (Birch et al., 1984Birch et al., 1984) in the near-field, and conversely closer in agreement with predictions farther downstream. This is most notable in test 8 in which discrepancies at

all three measurement points are large. Although not conclusive, these observations are indicative of the previously discussed possible shortcomings of the model.

5. CONCLUSIONS

A turbulent computational fluid dynamic model capable of predicting the near-field structure of high pressure releases of multi-phase carbon dioxide representative of those arising from an accidental pipeline puncture or rupture has been presented. This model incorporates a novel approach for the evaluation of the state variables of CO_2, as recently presented by Wareing et al. (2012). Validation of this model has been undertaken against new experimental data also reported herein, and gathered as part of the CO2PipeHaz project. Overall, the model developed has yielded an excellent level of agreement with measurements of the temperature characteristics of these jets, and good agreement with composition data in a number of comparisons.

It has been identified that two areas of improvement are required to ensure accurate representation of the complex physics observed in these release scenarios and developmental work is currently ongoing to address these issues. Firstly, a second-moment turbulence closure is required to represent the turbulence anisotropy, which is expected to correct errors in the predicted rates of mixing due to the two-equation model implemented. Secondly, the inclusion of particles within a Lagrangian framework is required to more accurately represent the thermophysical interactions between the phases. A model describing the motion of fluid and solid particles has been written into the code, and is currently under validation. Both droplet and particle populations are predicted through solutions of equations for the particle distribution function used for small particles, with a Lagrangian particle tracking routine employed for larger particles.

Additionally, it is clear from the predictions of these dense phase releases that significant solids are generated within the near-field of these jets, despite the release itself containing no dry ice. This is an important conclusion with respect to the future design of CO_2 pipelines and the consideration of the related hazards.

The safety issues surrounding the transport of CO_2 in pipelines are focussed on the questions of the toxicity of an accidental release and the fast decompression of a pipeline following a catastrophic extension of a crack initiated at a local puncture. Here, the case of pure CO_2 has been investigated, but the impact of the presence of annex gases and impurities was considered out of the scope of the present work. It is to be expected that a number of different impurities may be present in a captured CO_2 stream dependent upon the industrial source, and

the presence of these additional compounds, some of which are more toxic than CO_2 (e.g. SO_2, H_2S, etc.), can drastically affect the temperature and pressure fields in the immediate vicinity of a local leak, eventually leading to fast crack propagation and total pipe failure. Also, and depending on the interactions between the bulk CO_2 and impurities in the pipe, the dispersing cloud conditions could also be so strongly affected that its composition may differ significantly from the composition of the transported fluid, potentially leading to clouds that are more hazardous because of higher levels of toxics due to the mechanism of phase partitioning occurring just outside the pipe, very close to the leakage point.

The presence of impurities therefore has a notable effect on the phase behaviour of CO_2, and hence alters the near-field characteristics of any accidental release. The introduction of small amounts of N_2 into high pressure CO_2, for example, shifts the triple point towards higher pressures and lower temperatures. These variations modify the near-field of the dispersing jet in terms of its shock structure, temperature and pressure which in turn impact on the phase distribution of the dispersing CO_2 and impurities. It is therefore concluded that the next step in code development will be the extension of the methodologies discussed here to model the near-field structure and dispersion characteristics of releases of CO_2 mixtures containing impurities and trace elements typical of those found in CCS streams. This will include both a continuous phase fluid model, and as previously discussed, a discrete-phase model capable of representing the distribution and properties of solid and liquid particles in such releases. The latter is an important consideration given the unusual phase behaviour of CO_2, and its sublimation from solid form at atmospheric conditions.

6. NOMENCLATURE

Roman letters:

c	adiabatic sound speed
C	constant
C_v	specific heat at constant volume
d	diameter
E	total energy
G	grid
H	Helmholtz free energy / enthalpy
k	turbulence kinetic energy
m	mass
n	virtual origin displacement
M	Mach number
p	pressure
r	radial distance
R	universal gas constant
s	source term
S	entropy
T	temperature
t	time
u	velocity
U	internal energy per unit mass
v	molar volume
V	volume
x	downstream distance from release
y	vertical distance relative to release height
z	axial distance

Greek letters:

α	CO_2 condensed fraction
β	CO_2 fraction
δ_{ij}	Kronecker delta
ε	dissipation rate of k
γ	ratio of specific heats
μ	viscosity
ρ	density
τ	relaxation time
τ_{ij}	shear stress
ω	acentric factor

Subscripts:

a	air
0	reference state
$crit$	critical
g	gas
i	spatial indice
j	spatial indice
k	spatial indice
l	condensed phase
s	saturation
t	turbulent / triple point
v	vapour

Superscripts:

$\bar{A}$	Reynolds average
$\tilde{A}$	Favre average
A''	fluctuating component

7. ACKNOWLEDGEMENTS

The research leading to the results described in this paper has received funding from the European Union 7th Framework Programme FP7-ENERGY-2009-1 under grant agreement number 241346.

The paper reflects only the authors' views and the European Union is not liable for any use that may be made of the information contained herein.

8. REFERENCES

Bartosiewicz, Y., Mercadier, Y., Proulx, P., 2002. Numerical Investigations on Dynamics and Heat Transfer in a Turbulent Underexpanded Jet. AIAA Journal 40(11), 2257-2265.

Baz, A.M.E., 1992. Modelling Compressibility Effects on Free Turbulent Shear Flows, 5th Biennial Colloquium on Computational Fluid Dynamics, UMIST.

Birch, A.D., Brown, D.R., Dodson, M.G., Swaffield, F., 1984. The Structure and Concentration Decay of High Pressure Jets of Natural Gas. Combustion Science and Technology 36, 249-261.

Birkby, P., Page, G.J., 2001. Numerical predictions of turbulent underexpanded sonic jets using a pressure-based methodology. Proceedings of the Institution of Mechanical Engineers 215(G), 165-173.

Chen, Y.S., Kim, S.W., 1987. Computation of Turbulent Flows Using an extended k-epsilon Turbulence Closure Model. NASA. Document number CR-179204.

Chicago, U.o., 2010. Flash Center for Computational Science. Accessed 13/07/11. http://flash.uchicago.edu/site/flashcode/

CO2PipeHaz, 2009. Quantitative Failure Consequence Hazard Assessment for Next Generation CO_2 Pipelines: The Missing Link. Accessed 19/12/12. http://www.co2pipehaz.eu/

DIPPR, 2013. DIPPR 801 database. (http://www.aiche.org/dippr/)

Dixon, C.M., Gant, S.E., Obiorah, C., Bilio, M., 2012. Validation of Dispersion Models for High Pressure Carbon Dioxide Releases, IChemE Hazards XXIII. IChemE, Southport, UK, pp. 153-163.

Donaldson, C.D., Snedeker, R.S., 1971. A study of free jet impingement. Part 1. Mean properties of free and impinging jets. J. Fluid Mech. 45(2), 281-319.

Fairweather, M., Ranson, K.R., 2003. Modelling of Underexpanded Jets Using Compressibility-Corrected, k-ε Turbulence Models, in: Hanjalic, K., Nagano, Y., Tummers, M. (Eds.), Turbulence, Heat and Mass Transfer 4. Begell House, Inc., pp. 649-656.

Fairweather, M., Ranson, K.R., 2006. Prediction of underexpanded jets using compressibility-corrected, two-equation turbulence models. Prog. Comput. Fluid Dy. 6(1,2,3), 122-128.

Falle, S.A.E.G., 1991. Self-similar Jets. Mon. Not. R. Astron. Soc. 250, 581-596.

Falle, S.A.E.G., Giddings, J.R., 1993. Body capturing using adaptive cartesian grids, Numerical methods for fluid dynamics. 4. [Proceedings of an International Conference on Numerical Methods for Fluid Dynamics, held at Reading University in april 1992]. Oxford University Press, Oxford, pp. 337-343.

Harten, A., Lax, P.D., Leer, B.v., 1983. On Upstream Differencing and Godunov-type Schemes for Hyperbolic Conservation Laws. Society for Industrial and Applied Mathematics Review 25(1), 35-61.

Jacobson, M.Z., 1999. Fundamentals of Atmospheric Modelling, 1 ed. Cambridge University Press.

Jones, W.P., Launder, B.E., 1972. The Prediction of Laminarization with a Two-equation Model of Turbulence. Int. J. Heat Mass Tran. 15, 301-314.

Liu, L.-G., 1984. Compression and phase behavior of solid CO_2 to half a megabar. Earth Planet. Sc. Lett. 71, 104-110.

NIOSH, 1996. Documentation for Immediately Dangerous to Life or Health Concentrations (IDLHs) for Carbon Dioxide. Accessed 01/11/12.
http://www.cdc.gov/niosh/idlh/124389.html

Peng, D.-Y., Robinson, D.B., 1976. A New Two-Constant Equation of State. Ind. Eng. Chem. Fun. 15(1), 59-64.

Sarkar, S., Erlebacher, G., Hussaini, M.Y., Kreiss, H.O., 1991. The analysis and modelling of dilatational terms in compressible turbulence. J. Fluid Mech. 227, 473-493.

Span, R., Wagner, W., 1996. A New Equation of State for Carbon Dioxide Covering the Fluid Region from the Triple-Point Temperature to 1100 K at Pressures up to 800 MPa. J. Phys. Chem. Ref. Data 25(6), 1509-1596.

Viti, V., Schetz, J., 2005. Comparison of First and Second Order Turbulence Models for a Jet/3D Ramp Combination in Supersonic Flow, 43rd AIAA Aerospace Sciences Meeting and Exhibit. American Institute of Aeronautics and Astronautics, pp. 1-11.

Wareing, C.J., Woolley, R.M., Fairweather, M., Falle, S.A.E.G., 2013. A Composite Equation of State for the Modelling of Sonic Carbon Dioxide Jets. AICheE Journal. DOI: 10.1002/aic.14102
Witlox, H.W.M., Harper, M., Oke, A., 2009. Modelling of discharge and atmospheric dispersion for carbon dioxide releases. J. Loss Prevent. Proc. 22, 795-802.
Zeman, O., 1990. Dilational Dissipation: The Concept and Application in Modeling Compressible Mixing Layers. Phys. Fluids A-Fluid 2(2), 178-188.

9. FIGURE CAPTIONS

Figure 1. Schematic diagram of INERIS CO_2 release test rig including sensor configuration.

Figure 2. General view of experimental rig, including filling sphere, main vessel and discharge pipe.

Figure 3. Pressure vessel instrumentation.

Figure 4. Example of orifice flange.

Figure 5. High-speed camera still of a 9mm release.

Figure 6. Predicted normalised axial centre-line velocity of a highly under-expanded air jet obtained using a standard and a compressibility-corrected k-ε turbulence model, plotted against experimental data.

Figure 7. CO_2 internal energy predictions on the saturation line using the composite equation of state, showing gaseous and dense phases.

Figure 8. Adaptive mesh refinement grid mapped onto velocity predictions in the region of a Mach disc.

Figure 9. Predictions (lines) of axial temperature and O_2 mole fraction profiles (not test 4) plotted against experimental data (symbols) for tests 2, 3, and 4.

Figure 10. Predictions (lines) of vertical temperature profiles plotted against experimental data (symbols) for tests 6, 7, and 8, at axial locations of 1, 2 and 5 m.

Figure 11. Predictions (lines) of axial temperature and O_2 mole fraction profiles plotted against experimental data (symbols) for tests 6, 7, and 8.

10. TABLE CAPTIONS

Table 1. Parameters of the experimental releases.

Figure 01

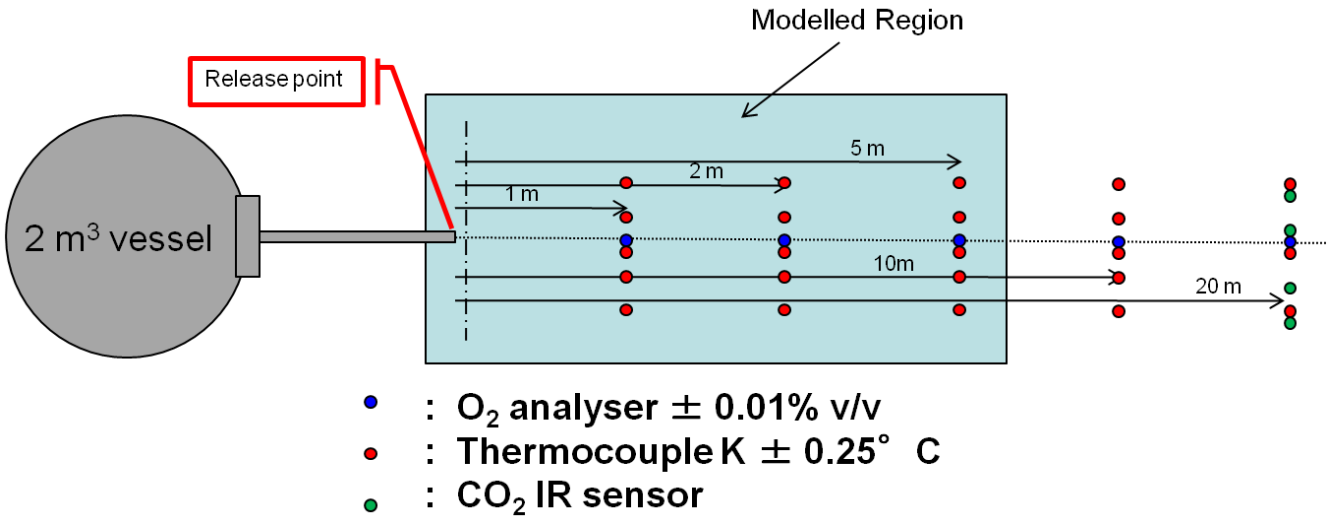


Figure 02



Figure 03

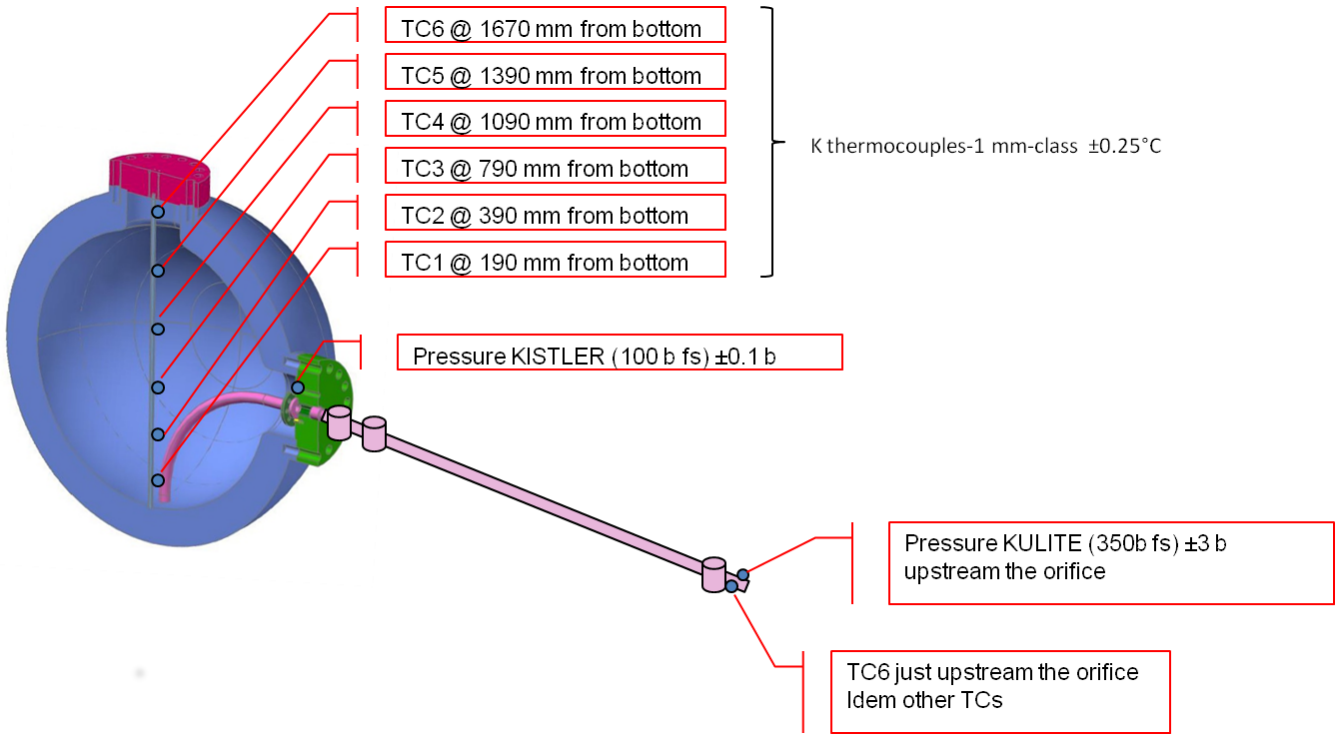


Figure 04

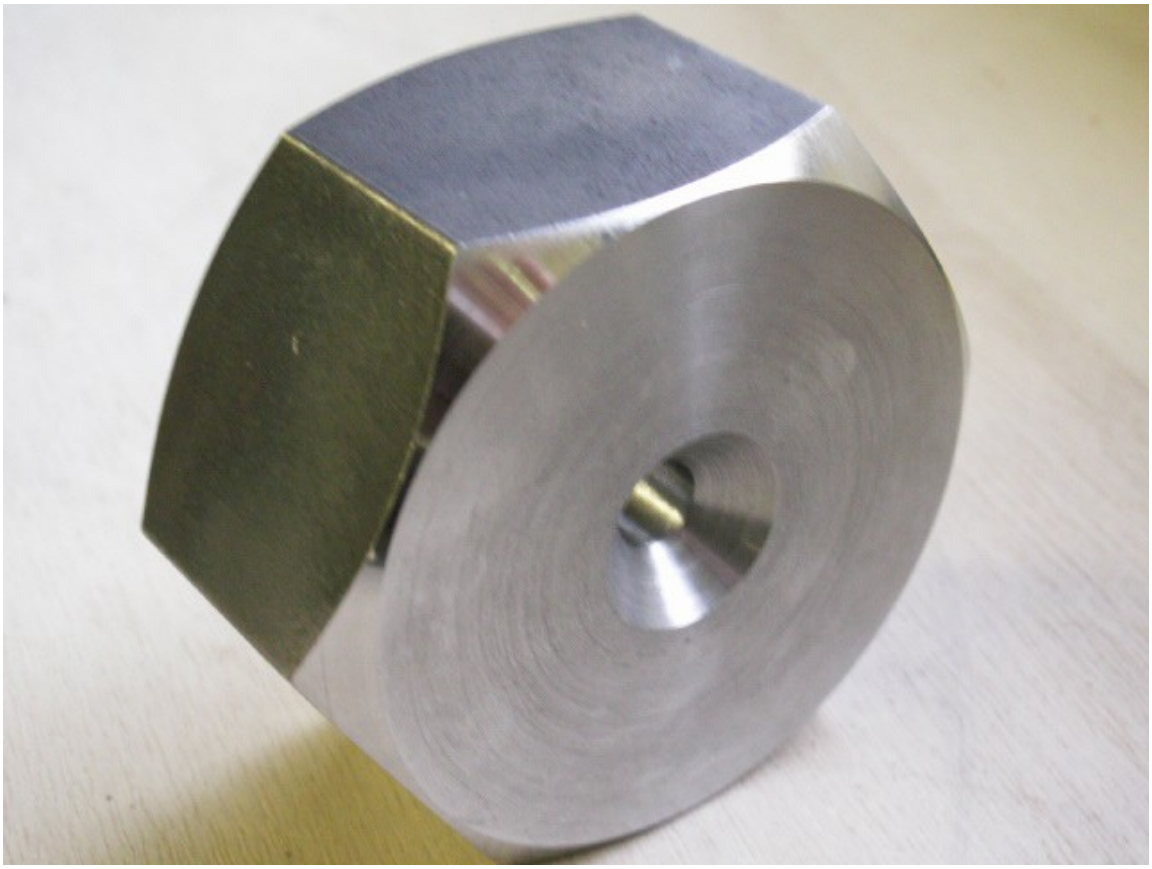


Figure 05



Figure 06

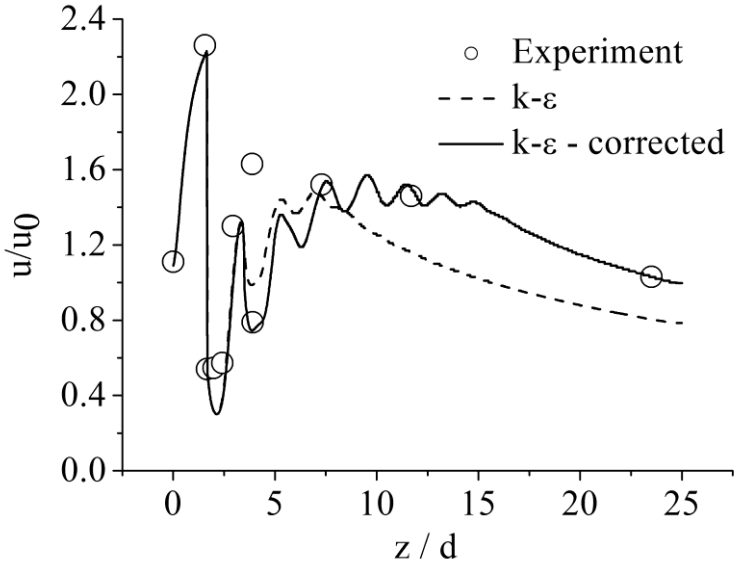


Figure 07

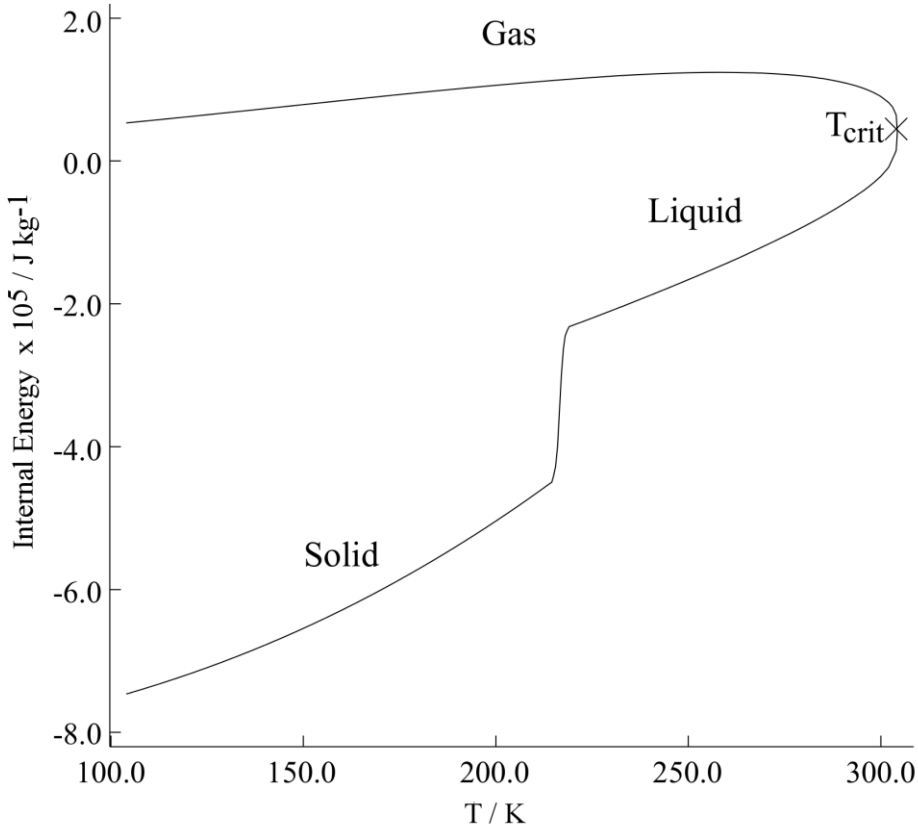


Figure 08

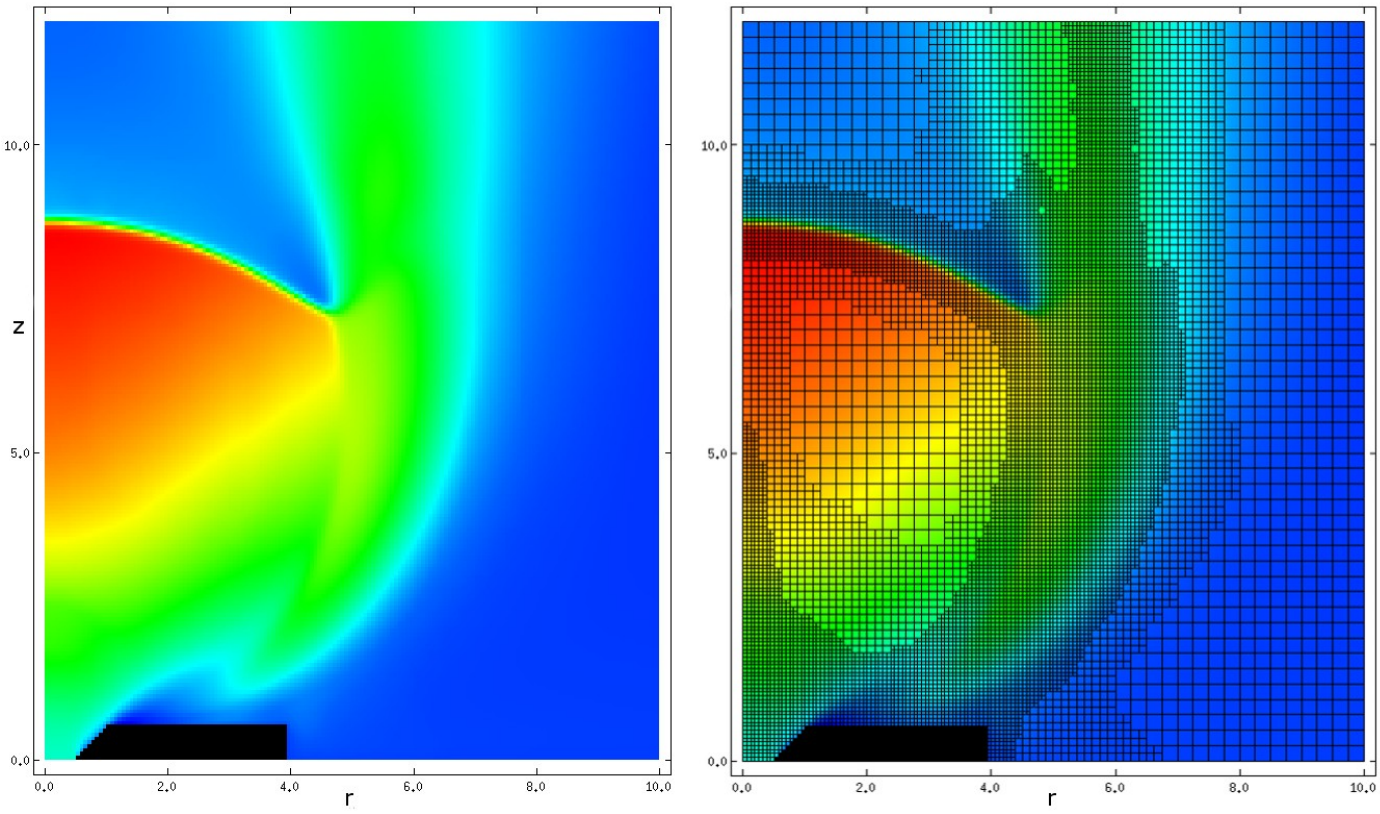
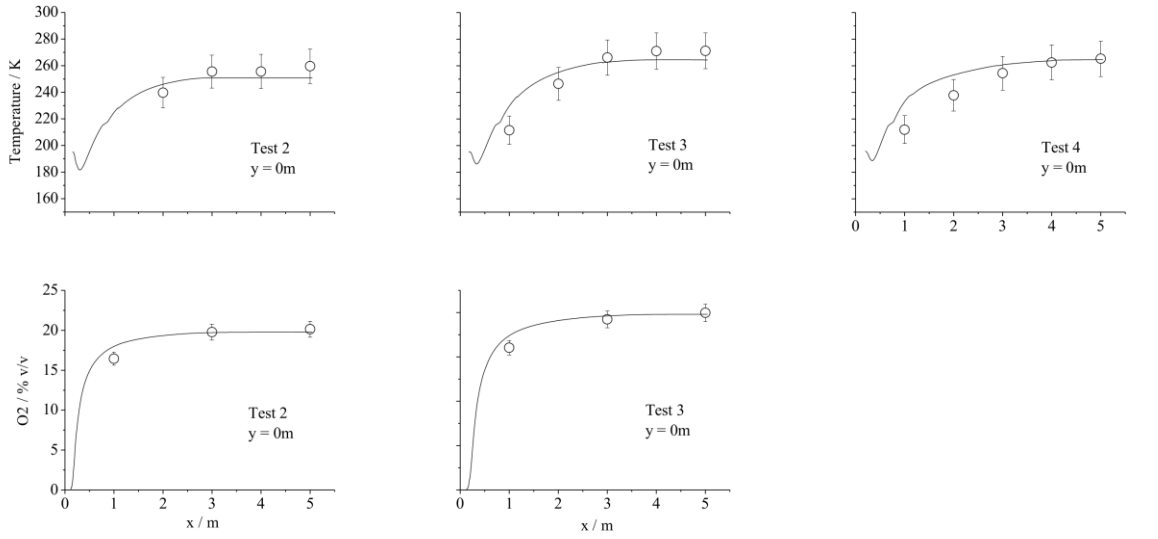


Figure 09



Test 2	Test 3	Test 4
Pressure = 28.4 bar, diameter = 6 mm	Pressure = 44.8 bar, diameter = 6 mm	Pressure = 39 bar, diameter = 6 mm

Figure 10

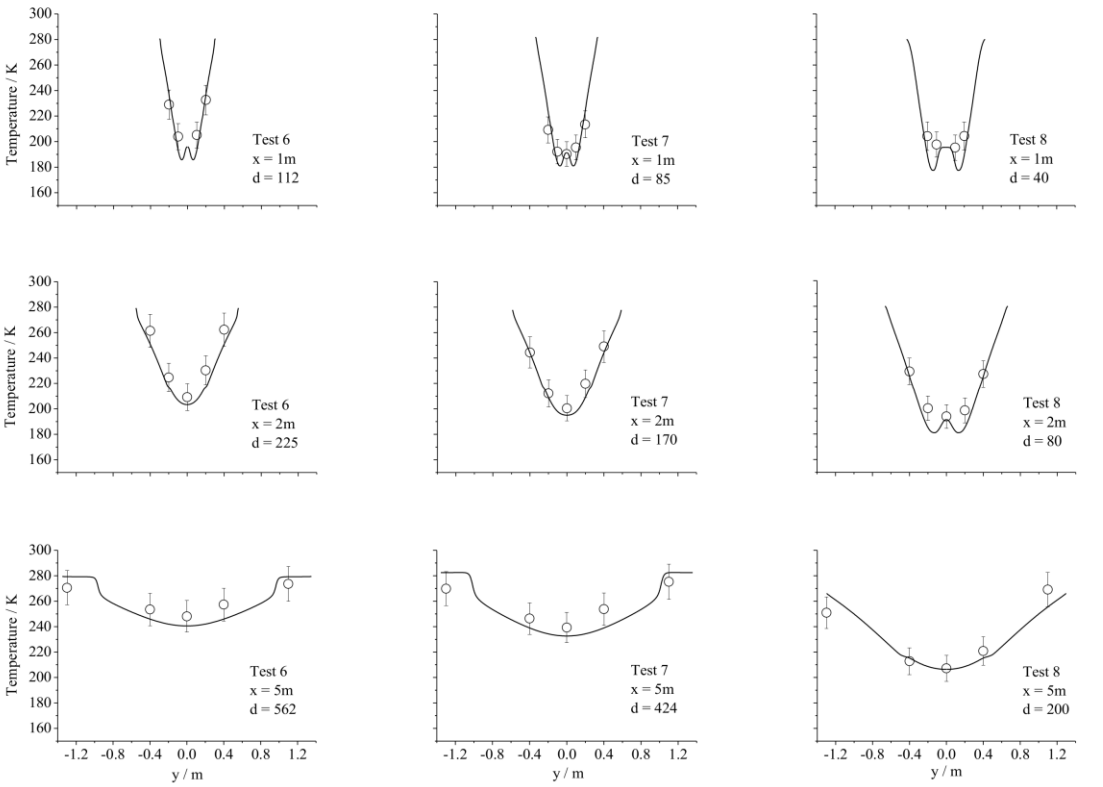


Figure 11

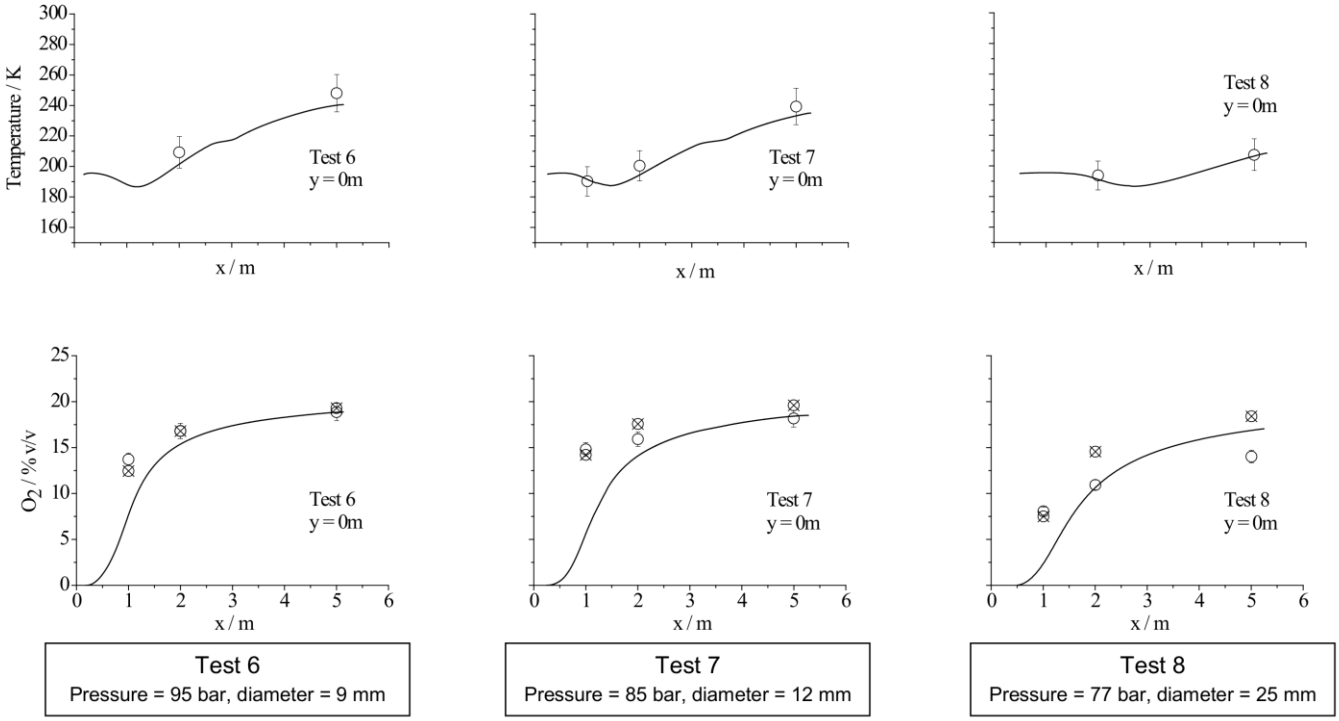


Table 01

Test Number	Ambient Temperature / K	Air Humidity / %	Reservoir Pressure / bar	Nozzle Diameter / mm
2	272.15	90.0	28.4	6
3	281.65	90.0	44.8	6
4	278.35	90.0	39.0	6
6	276.15	95.0	95.0	9
7	279.15	95.0	85.0	12
8	277.15	95.0	77.0	25